crystals

MDPI

Article

Integrated Prediction of Gas Metal Arc Welding Multi-Layer Welding Heat Cycle, Ferrite Fraction, and Joint Hardness of X80 Pipeline Steel

Chen Yan [1,2,†], Haonan Li [3,†], Die Yang [1,2], Yanan Gao [4], Jun Deng [1], Zhihang Zhang [3] and Zhibo Dong [3,*]

[1] China Petroleum Pipeline Research Institute Co., Ltd., Langfang 065000, China; yanchen@cnpc.com.cn (C.Y.); yangdie@cnpc.com.cn (D.Y.); yjydj@cnpc.com.cn (J.D.)
[2] National Engineering Research Center for Oil and Gas Pipeline Transportation Safety, Langfang 065000, China
[3] National Key Laboratory of Precision Welding and Joining of Materials and Structures, Harbin Institute of Technology, Harbin 150001, China; 22s009126@stu.hit.edu.cn (H.L.); 23b909142@stu.hit.edu.cn (Z.Z.)
[4] PipeChina Engineering Technology Innovation Co., Ltd., Tianjin 300450, China; gaoyn01@pipechina.com.cn
* Correspondence: dongzhb@hit.edu.cn
† These authors contributed equally to this work.

Abstract: X80 pipeline steel is widely used in oil and gas pipelines because of its excellent strength, toughness, and corrosion resistance. It is welded via gas metal arc welding (GMAW), risking high cold crack sensitivities. There is a certain relationship between the joint hardness and cold crack sensitivity of welded joints; thus, predicting the joint hardness is necessary. Considering the inefficiency of welding experiments and the complexity of welding parameters, we designed a set of processes from temperature field analysis to microstructure prediction and finally hardness prediction. Firstly, we calculated the thermal cycle curve during welding through multi-layer welding numerical simulation using the finite element method (FEM). Afterwards, BP neural networks were used to predict the cooling rates in the temperature interval that ferrite nuclears and grows. Introducing the cooling rates to the Leblond function, the ferrite fraction of the joint was given. Based on the predicted ferrite fraction, mapping relationships between joint hardness and the joint ferrite fraction were built using BP neural networks. The results shows that the error during phase fraction prediction is less than 8%, and during joint hardness prediction, it is less than 5%.

Keywords: X80 pipeline steel; multi-layer welding numerical simulation; BP neural network; phase fraction prediction; joint hardness prediction

check for updates

Academic Editor: José L. García

Received: 25 November 2024
Revised: 16 December 2024
Accepted: 24 December 2024
Published: 26 December 2024

Citation: Yan, C.; Li, H.; Yang, D.; Gao, Y.; Deng, J.; Zhang, Z.; Dong, Z. Integrated Prediction of Gas Metal Arc Welding Multi-Layer Welding Heat Cycle, Ferrite Fraction, and Joint Hardness of X80 Pipeline Steel. *Crystals* **2025**, *15*, 14. https://doi.org/10.3390/cryst15010014

1. Introduction

X80 pipeline steel has gained significant attention for its exceptional strength, toughness, and corrosion resistance, making it the material of choice for constructing oil and gas pipelines worldwide [1–3]. The high performance of X80 steel in such demanding applications is critical, particularly in areas prone to harsh environmental conditions [4]. However, welding this material, typically through gas metal arc welding (GMAW), presents challenges due to its high sensitivity to cold cracking, which can significantly compromise the integrity of the welded joint [5].

The relationship between joint hardness and the cold crack susceptibility of welded joints has been well documented [6]. Therefore, accurately predicting the hardness of the weld is of paramount importance for ensuring the reliability and durability of welded pipeline joints. Traditionally, experimental methods have been employed to determine joint hardness, but these approaches are not only time-consuming but also costly, given the multitude of welding parameters involved [7].

In response to these challenges, some scholars have carried out related research in the field of hardness prediction. Vignesh et al. [8] predicted the hardness of magnesium alloy by establishing a finite element model. The prediction process is to simulate the Rockwell hardness measurement process. The hardness of the material can be obtained by inputting the corresponding material and indenter parameters. Murali et al. [9] conducted a large number of friction stir welding experiments and obtained a large amount of joint data on friction stir welding by changing the process parameters. After summarizing the data, the prediction model of the friction stir welding of the material from the process parameters to the joint performance was obtained. Guo et al. [10] realized the prediction of hardness based on the microstructure and composition of high-entropy alloys. This method can be used to predict the hardness and other properties of high-entropy alloys with known components. Almeida et al. [11] used a combination of optical parameters and neural network training to realize the hardness prediction of ore. Kasuya et al. [12] studied the relationship between Ac1, Ac2 values and HAZ hardness in the heat-affected zone of the weld and finally obtained an empirical equation to predict the decrease in tempering hardness and the change in precipitation hardness.

However, the existing research has mainly focused on modeling specific processes related to the evolution of the microstructure in the weld joint. In actual welding, joint hardness is essentially influenced sequentially by the welding process temperature field microstructure hardness [13–16]. Moreover, in industrial production, joint hardness is typically adjusted by altering the welding parameters. Directly establishing a mapping relationship between welding parameters and joint hardness may neglect the impact of the temperature field and microstructural changes, which limits the scalability and applicability of prediction models [17–19].

On this basis, this study propose a comprehensive approach that integrates process simulation, microstructure prediction, and machine learning techniques to predict the joint hardness of X80 steel welded joints. This methodology provides a more efficient and accurate alternative to traditional experimental procedures. Initially, the thermal cycle during the welding process is analyzed through numerical simulation using the finite element method (FEM). The resulting data provide critical insights into the temperature distribution and cooling rates, which are pivotal in determining the resulting microstructure of the weld.

To further enhance the predictive accuracy, we employ backpropagation (BP) neural networks to model the cooling rates within the temperature range that influences ferrite nucleation and growth. These cooling rates are then incorporated into the Leblond function to estimate the ferrite fraction of the welded joint. Finally, the relationship between joint ferrite fraction and hardness is established using BP neural networks, providing a robust tool for predicting the hardness of X80 steel welds.

The proposed approach offers a promising solution for reducing the reliance on experimental trials, thereby accelerating the development of high-quality welded joints in pipeline applications. Additionally, the welding process temperature field microstructure hardness sequential prediction network has strong scalability. It can be extended to different application scenarios by modifying a specific sequential model.

2. Problem Formulation

To predict the hardness of the joint, empirical formula methods can be used, or a nonlinear mapping relationship between the joint hardness and the upper-level factors can be established using artificial neural networks. However, most empirical equations currently require material constitutive parameters, which are often difficult to measure. Therefore, constructing an artificial neural network is a feasible approach [7]. Considering that welding process parameters affect the welding thermal cycle, which in turn influences the joint microstructure and subsequently the joint hardness, the network construction can take into account the establishment of a process thermal field microstructure hardness cascade network.

The composition of the overall prediction network is discussed in a bottom-up manner. The acquisition of microstructure information is considered firstly. Common methods for acquiring microstructure information include analytical methods such as the Leblond function and JMA-K equation [20,21], as well as numerical methods such as Monte Carlo simulations [22], cellular automata [23], phase field methods [24], and molecular dynamics simulation [25]. Given the need for network efficiency, it is appropriate to use analytical equations to solve for microstructure information. Among these, the Leblond function is based on the Continuous Cooling Transformation (CCT) curve and is an iterative calculation function for phase fractions [26,27], while the JMA-K equation provides an analytical expression for phase fraction variation with time under isothermal conditions. Since phase transformation in welded joints typically occurs under rapid cooling conditions, this study prefers to use the Leblond function, which is based on continuous cooling kinetics, to solve for phase fractions.

The prediction of joint microstructure fractions relies on the temperature field information of the welding cooling process. In most studies, temperature field information can be obtained using thermocouples. However, for welding processes, especially at the weld seam location, which involves solid–liquid–solid phase transitions, it is difficult to fix the thermocouple, making temperature field measurements challenging. A reliable solution is to combine the finite element method (FEM) to calculate the welding temperature field, then compare the temperature field calculation results from the heat-affected zone with experimental results. Based on this comparison, the temperature field at the weld seam location can be extracted.

However, for each welding process, if the finite element method (FEM) is used to calculate the temperature field (which can be replaced by the thermal cycle curve in welding), the time cost is quite high. Therefore, using existing samples and combining machine learning techniques to predict the thermal cycle curve under varying process conditions is clearly a more efficient and optimal choice.

To summarize the above problem formulation, we propose the prediction network shown in Figure 1. First, the welding thermal cycle curve is calculated using the finite element method (FEM) and used as the initial sample. A nonlinear mapping model between the process and thermal cycle curve is then established using an artificial neural network. The thermal history is input into the Leblond function to obtain the phase fraction. A phase fraction-to-joint hardness mapping model is established to predict the hardness of the welding joint under different process conditions.

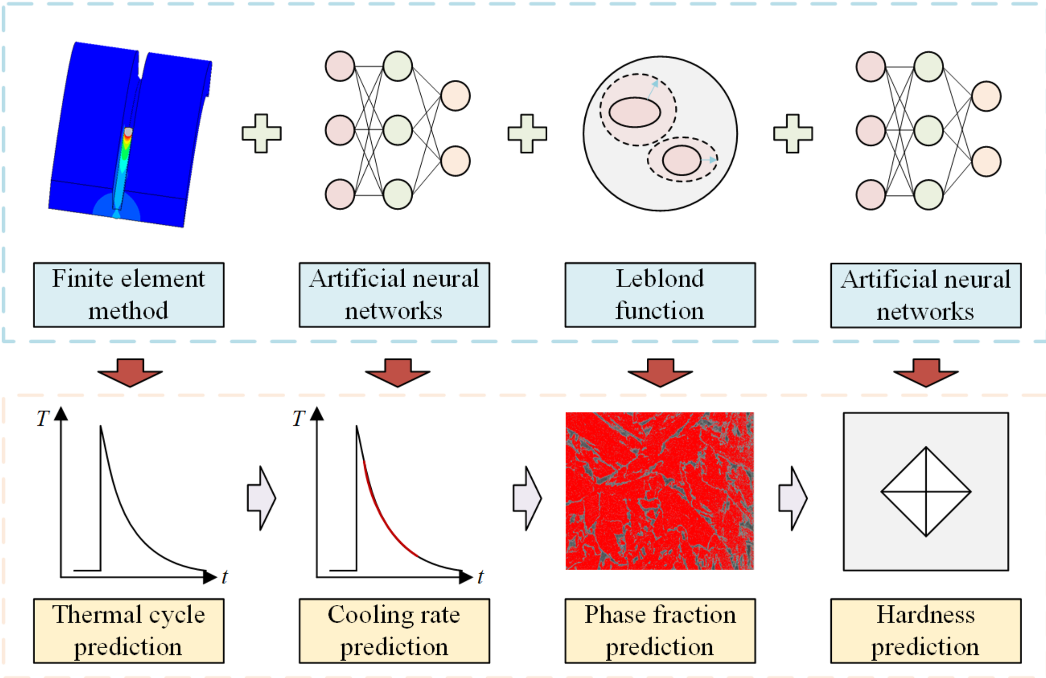

Figure 1. Hardness prediction flow chart of X80 pipeline steel.

3. Algorithm and Models

In this section, the mentioned algorithm and models will be introduced. Furthermore, the specific settings during the hardness prediction will be given.

3.1. Finite Element Method

The finite element method is achieved via geometric modeling, meshing, and numeric iteration. Firstly, we use software Solidworks 2018 to establish a three-dimensional geometric according to the actual joint size. After that, the three-dimensional model is imported into the software Hypermesh 14.0 for meshing. The microstructures and hardness changes acutely in or near the welding pool, so we use hexahedral elements with a side length of 1mm to mesh the region. In the area whose microstructures and hardness is less affected by the welding temperature field, such as the base metal far away from the pools, the elements are divided into larger ones to reduce the whole element quantity. Elements that gradually increase in size are introduced from the pool to the base metal.

To proceed, the elements are introduced to the software MSC.Marc 2018 for numeric iterating. To obtain a more accurate temperature field, the thermal physical performance parameters include specific heat, heat conductivity, coefficient of thermal expansion, elasticity modulus, and yield strength, which are imported in tabular form. The parameters will be introduced later. Next, the boundary conditions are set, and the preheating temperature between the layers is set to 80 °C according to the actual processing. The double ellipsoid model is selected as the heat source, and the parameters of the double ellipsoid model are set based on the actual measured pool morphologies. The welding process and interlayer cooling process of the welds are defined as working conditions and added to the analysis task in turn according to the actual GMAW multi-layer welding process. After completing the GMAW multi-layer welding condition setting, the finite element model is submitted for thermal analysis numerical calculation, and the temperature field cloud map of each incremental step in the welding process can be obtained.

3.2. Leblond Function

The Leblond function, a major predicting model adopted in the software Sysweld 2019, can predict the phase fraction evolution considering phase growth dynamics. The govern function is written as follows:

$$\frac{dp}{dt} = f(\dot{T}) \frac{p_{eq}(T) - p}{\tau(T)} \quad (1)$$

where p is the phase volume fraction at the moment, t is the time, $f(\dot{T})$ is the correction factor, $p_{eq}(T)$ is the equilibrium volume fraction at the temperature, and $\tau(T)$ is the relaxation time, which is a function of temperature. Its physical meaning is the start time of the phase transition. The method that confirms these parameters is given in our previous work [26].

In the welding process, phase transition occurs during cooling. Based on the above analysis, we express the phase fraction at $t = i$ by p_i, and the phase fraction at the next moment p_{i+1} can be expressed as follows:

$$p_{i+1} = p_i + \frac{dp}{dt} \Delta t \quad (2)$$

The temperature at the moment can be written as follows:

$$T_{i+1} = T_i + V_c(t) \Delta t \quad (3)$$

where $V_c(t)$ is the cooling rate. With certain Leblond parameters $f(\dot{T})$, $p_{eq}(T)$, and $\tau(T)$, the phase fraction after welding can be predicted using iteration traversing the cooling time.

The transition start and end temperatures are required to determine the Lebond parameters. However, the cooling rate will affect the critical temperature at which the phase transition starts or ends. A CCT diagram analysis would be beneficial. To simplify, we select the medium temperature at which the phase transition starts and ends at different cooling rates as the critical temperature, respectively. Due to the simplification of $\tau(T)$ and $p_{eq}(T)$, $f(\dot{T})$ is required to fix the subsequent errors. $f(\dot{T})$ always changes unevenly at different cooling rates, and the regularity of the fitted curve is not strong. Therefore, the phase fraction under different cooling rates in CCT curves is needed so that the $f(\dot{T})$ can be fitted. After that, we can obtain the $f(\dot{T})$ under the actual cooling rate via interpolation.

3.3. Artificial Neural Networks

The prediction of thermal cycling curves and joint hardness essentially involves establishing a nonlinear mapping relationship between these outputs and the upper-level input variables. In this study, the upper-level inputs are the primary influencing factor data. To guarantee the efficiency of data transmission, a backpropagation (BP) neural network is employed for modeling. This section first introduces the BP neural network algorithm and subsequently discusses the structures of the prediction networks for thermal cycling curves and joint hardness in detail.

3.3.1. BP Neural Network

The BP neural network is a type of multilayer feedforward neural network based on the error backpropagation algorithm. By utilizing an input layer, hidden layers, and an output layer, it performs nonlinear mapping of data and is capable of learning complex functional relationships. During the training process, the BP algorithm adjusts the weights and biases within the network based on the output error to minimize the error function. Its typical structure is shown in Figure 2.

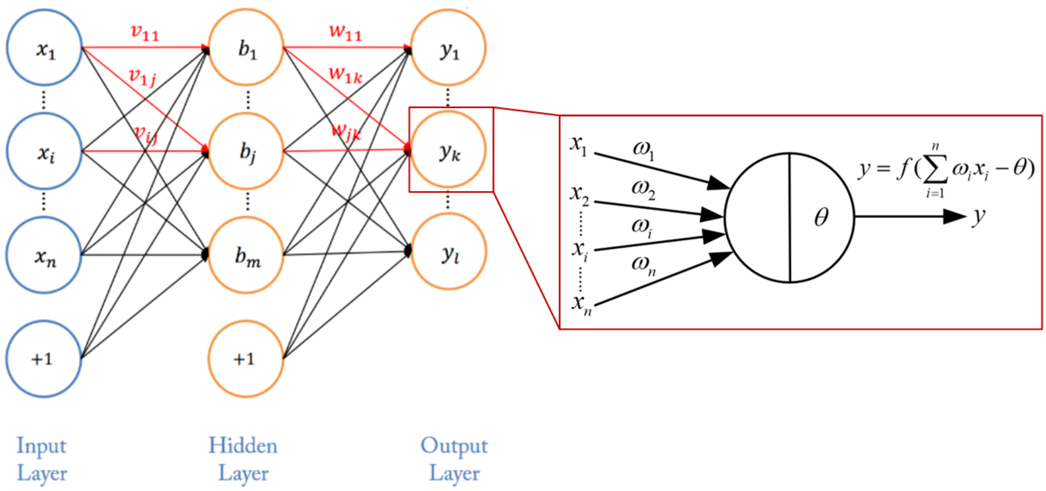

Figure 2. A schematic diagram of the typical structure of a BP neural network.

The computation process of a BP neural network consists of forward propagation and backward propagation. For the fully connected network shown in Figure 2, the forward propagation process involves each neuron applying a weighted sum to the outputs of the neurons in the preceding layer, subtracting the bias of the neuron and then passing the result through an activation function to obtain the output of that neuron. Here, v_{ij} represents the weight between input layer neuron i and hidden layer neuron j, and w_{jk} represents the weight between hidden layer neuron j and output layer neuron k. The bias of the neurons is written by θ. x_i is the output of the i-th input layer neuron, b_j is the output of the j-th hidden layer neuron, and y_k is the output of the i-th output layer neuron. The Sigmoid function is chosen as the activation function to map the linear combination of inputs to a nonlinear output, allowing the network to learn and represent complex nonlinear relationships.

To ensure the prediction accuracy of the network, it is necessary to train the weights and biases of each neuron through backpropagation, ensuring that the final network output error is smaller than the desired value. The training method selected in this study is the gradient descent method. The gradient of the weights between the hidden layer and the output layer $\nabla\omega_{jk}$ is given as follows:

$$\nabla\omega_{jk} = \frac{\partial E}{\partial \omega_{jk}} = \frac{\partial E}{\partial y_k}\frac{\partial y_k}{\partial \beta_k}\frac{\partial \beta_k}{\partial \omega_{jk}} \tag{4}$$

where β_k is the output received by neuron k from the previous layer, and E is the Mean Squared Error (MSE), determined by the desired output T_k and the actual output y_k

$$E = \frac{1}{2}\sum_k (T_k - y_k)^2 \tag{5}$$

In Equation (4):

$$\frac{\partial E}{\partial y_k} = y_k - T_k \tag{6}$$

$$\frac{\partial y_k}{\partial \beta_k} = f'(\beta_k - \theta_k^y) = f(\beta_k - \theta_k^y)[1 - (\beta_k - \theta_k^y)] = y_k(1 - y_k) \tag{7}$$

$$\frac{\partial \beta_k}{\partial \omega_{jk}} = b_j \tag{8}$$

By simultaneously solving Equations (4)–(8), we can obtain the following:

$$\nabla\omega_{jk} = y_k(1-y_k)(y_k - T_k)b_j \tag{9}$$

The weights ω_{jk} updates as follows:

$$\omega_{jk} = \omega_{jk} + \eta\nabla\omega_{jk} \tag{10}$$

where η is the learning rate, which is set to 0.01 in this study.

The bias of the output layer can be expressed as follows:

$$\nabla\theta_k^y = \frac{\partial E}{\partial\theta_k^y} = \frac{\partial E}{\partial y_k}\frac{\partial y_k}{\partial\theta_k^y} \tag{11}$$

here,

$$\frac{\partial y_k}{\partial\theta_k^y} = -f'(\beta_k - \theta_k^y) = -y_k(1-y_k) \tag{12}$$

Therefore, we can obtain the gradient of the bias:

$$\nabla\theta_k^y = -y_k(1-y_k)(y_k - T_k) \tag{13}$$

The bias will be later update as follows:

$$\theta_k^y = \theta_k^y + \eta\nabla\theta_k^y \tag{14}$$

The gradient of the weights between the input layer and the hidden layer ∇v_{ij} is given as follows:

$$\nabla v_{ij} = \frac{\partial E}{\partial v_{ij}} = \frac{\partial E}{\partial b_j}\frac{\partial b_j}{\partial v_{ij}} \tag{15}$$

here

$$E = \frac{1}{2}\sum_k (T_k - y_k)^2 = \frac{1}{2}\sum_k \left(T_k - f(\sum_{j=1}^{m}\omega_{ij}b_j - \theta_j^y)\right)^2 \tag{16}$$

$$\frac{\partial E}{\partial b_j} = \sum_{k=1}^{l} y_k(1-y_k)(T_k - y_k)\omega_{jk} \tag{17}$$

$$\frac{\partial b_j}{\partial v_{ij}} = b_j(1-b_j)x_i \tag{18}$$

By simultaneously solving Equations (15)–(18), the weight gradients can be obtained:

$$\nabla v_{ij} = \sum_{k=1}^{l} y_k(1-y_k)(T_k - y_k)\omega_{jk}b_j(1-b_j)x_i = \sum_{k=1}^{l}\nabla\omega_{jk}\omega_{jk}b_j(1-b_j)x_i \tag{19}$$

Subsequently , the weights between the input layer and the hidden layer are updated as follows:

$$v_{ij} = v_{ij} + \eta\nabla v_{ij} \tag{20}$$

The gradient of the bias in the hidden layer is given as follows:

$$\nabla\theta_j^b = \frac{\partial E}{\partial \theta_j^b} = \frac{\partial E}{\partial b_j}\frac{\partial b_j}{\partial \theta_b^j} \tag{21}$$

where

$$\frac{\partial b_j}{\partial \theta_j^b} = -b_j(1-b_j) \tag{22}$$

By substituting Equation (22) into Equation (21), we can obtain the following:

$$\nabla\theta_j^b = \sum_{k=1}^{l} -y_k(1-y_k)(T_k-y_k)b_j(1-b_j) = \nabla\theta_k^y b_j(1-b_j) \tag{23}$$

The bias can be updated as follows:

$$\theta_j^b = \theta_j^b + \eta\nabla\theta_j^b \tag{24}$$

Before constructing the neural network, it is necessary to divide the training samples into training and testing samples. The training samples are used for the basic data propagation, while the testing samples serve as the accuracy criterion for the current iteration. Additionally, the weights and biases obtained during training need to be stored for direct use in subsequent prediction processes.

3.3.2. Cooling Rate Predicting Networks

The cooling rate of the joint is influenced by key parameters such as welding current, welding voltage, and welding speed. Therefore, it is feasible to establish a mapping model between these welding parameters and the cooling rate. However, since the cooling rate is a time-varying quantity, this leads to a significant increase in the number of training samples. To improve training efficiency, this study proposes the following prediction method: the cooling segment of the thermal cycle curve is expressed by a function, and the key parameters of this function are trained using a BP neural network to obtain the complete cooling segment. Subsequently, the cooling rate at each time step is obtained via differentiation.

To proceed, we deduce the expressing function. For the selection of the mathematical function representing the temperature–time curve of the cooling process in welding, it can be simplified to calculate the cooling process of a high-temperature metal block. The conclusions derived from this simplified calculation can then be extended to the welding process temperature variation. According to the principles of heat transfer, the rate at which a hot object radiates heat to its surrounding environment is proportional to the temperature difference between the object and the surrounding environment, as described by Newton's Law of Cooling. Therefore, from the perspective of convective heat transfer, it can be mathematically expressed as follows:

$$\frac{dQ}{dt} = h \times A \times (T - T_s) \tag{25}$$

here, dQ/dt represents the rate of heat loss from the metal block, h is the heat transfer coefficient, A is the surface area of the metal block, and T_s is the environmental temperature. Assuming the metal block is isotropic and homogeneous, with the exception of the surface, the rest of the block is insulated, and the lumped parameter method can be used to describe the cooling process of the high-temperature metal block. This method assumes that the entire block can be treated as a single homogeneous entity with a uniform temperature. Using the lumped capacitance method and the aforementioned equations, the function expression for the temperature of the metal block as a function of time during the cooling process can be derived. This function takes the form of exponential decay, expressed as follows:

$$T(t) = T_0 + (T_s - T_0) \times \exp(\frac{-h \times A \times t}{m \times C_p}) \tag{26}$$

where T_0 is the initial temperature, m is the weight of the block, and C_p is the specific heat capacity. According to the basic form of Equation (26), we give an approximate fuzzy equation to adapt to the welding cooling conditions.

$$T(t) = T_H \exp[-b \times (t - c)] + T_0 \tag{27}$$

Here, T_H is the mathematical function adjustment parameters based on the initial temperature, T_0 is the mathematical function adjustment parameters based on the ambient temperature, b is the adjustment parameters for the curvature of the temperature decline curve, and c is the adjustment parameters for shifting the function along the x-axis, which are used to fit the multi-pass welding scenario. It should be noted that T_H and T_0 in the equation are not the actual peak temperature and ambient temperature but are parameters used for the fitting function. Their numerical values will be close to the peak temperature or ambient temperature, but they have no practical significance. We can obtain the cooling curve by establishing a nonlinear mapping model between the welding current, welding voltage, welding speed, and T_H, b, and c. Subsequently, the cooling rate at each incremental step can be obtained by differentiating the curve.

3.3.3. Hardness Predicting Networks

Hardness is mainly decided by microstructure components. Therefore, using the volume fraction of the main phases as the network input and local hardness as the output is appropriate.

The process parameters of multi-layer welding and the microstructure information of each welding layer correspond to the hardness values of each welding layer, respectively. According to the same information above, a multi-layer network is constructed based on the BP algorithm. The actual measured hardness data of each welding layer are divided into a training set and test set of the strength prediction neural network. The training set is used to calculate the threshold and weight of the hardness neural network of multi-layer welding joints, and the test set is used to test the prediction results of the hardness values of each welding layer.

In the design of the neural network, the BP algorithm is used to construct a multi-layer network to train the weights of nonlinear differentiable functions. By changing the scale and connection weights in the neural network, the nonlinear classification problem can be effectively processed, and all nonlinear functions can be solved with arbitrary accuracy. These data are stored in the *.txt* document in the form of a matrix and read by the *if-stream* statement to ensure the accurate import of the training data.

In the training process, according to the principle of gradient descent, a loop statement is written to convert the calculation formula into code to realize the training of the threshold and weight of each neuron in the hardness neural network of multi-layer welded joints. Through the change in MSE, the network parameters are continuously optimized until the predetermined training goal is achieved.

After completing the hardness prediction part of the welded joint, the strength parameters of the welded joint are trained in the same way. The actually measured tensile strength and shear strength of the welded joint are used as the training set and test set of the strength prediction neural network to explore the strength of the welded joint. The relationship with the structure until the joint strength prediction within the predetermined error range can be achieved.

4. Dataset Preparation

As introduced in Section 3, most of the algorithms and models are data-driven. Therefore, experimental methods are required to measure the necessary data. The finite element simulation requires specific heat, thermal conductivity, coefficient of thermal expansion, elastic modulus, and yield strength at different temperatures to define the material properties. The results need to be verified using the weld pool morphology and the thermal cycle curves at typical locations. The Leblond equation requires the material's CCT diagram and the phase fraction results under different welding conditions. The prediction of joint hardness requires hardness data under different welding processes as the training set.

4.1. GMAW Multi-Layer Welding and Welding Thermal Cycle Curve Measuring

The test substrate is API 5L X80 pipeline steel, with an outer diameter of 1219 mm and a wall thickness of 22 mm. The electrode used in the test was Austrian BOHLER SG 8-P pipeline welding wire, and the electrode model was ER80S-G gas protection welding wire. Their compositions are listed in Table 1 and Table 2, respectively.

Table 1. Chemical compositions of X80 pipeline steel (wt.%).

C	Si	Mn	P	S	Ni	Cu	Nb	Ti	Mo	Cr	Ce
0.05	0.23	1.64	0.015	0.002	0.18	0.05	0.06	0.018	0.21	0.23	0.17

Table 2. Chemical compositions of BOHLER SG 8-P pipeline welding wire (wt.%).

C	Si	Mn	P	S	Mo	Ni	V	Cu	Ti	Al	Zr
0.07	0.70	1.58	0.006	0.008	0.01	0.87	0.01	0.04	0.08	0.01	0.01

In this experiment, the multi-layer welded joint groove uses a composite groove commonly used in pipeline engineering, as shown in Figure 3a. In the welding process of thick-walled pipelines (especially when the wall thickness exceeds 12 mm), this groove design can reduce the amount of filler metal required for the weld and the heat input during welding, thus significantly improving production efficiency and greatly reducing the probability of welding defects. The specific parameters in the figure are as follows: the groove face angle β is set to $5 \pm 1.0°$, the angle α is $45 \pm 1.0°$, the angle γ is $37.5 \pm 1.0°$, the root face (P) dimension is 1.1 ± 0.2 mm, no backing material is required, and the root gap (b) is controlled within the range of 0 to 0.5 mm. The height (H) from the inflection point to the inner wall of the pipe is set to 5.1 ± 0.2 mm. The width (W) of the semi-groove is between 3.9 mm and 4.3 mm. The height (h) of the internal groove is set to 1.7 ± 0.2 mm, and the residual height of the joint is controlled between 0 and 2.0 mm. A residual height exceeding 2.0 mm is allowed in regions with a local length not exceeding 50 mm, but it must not exceed 3.0 mm.

The welding method is GMAW, and the girth weld is composed of nine layers of welds. From the inner wall to the outer wall of the pipe, it is root welding, hot welding, five-pass filling welding, and two-pass cover welding. Among them, filling one, two, three, or four welds, or covering one or two welds, are achieved by the double welding torch at the same time. The cross section is shown in the main view of the model in Figure 3b, and the welding parameters of the welds are listed in Table 3. In each welding process, K-type thermocouples are used to measure the thermal cycle curve of each weld. The placement position of the thermocouple is shown in Figure 3c.

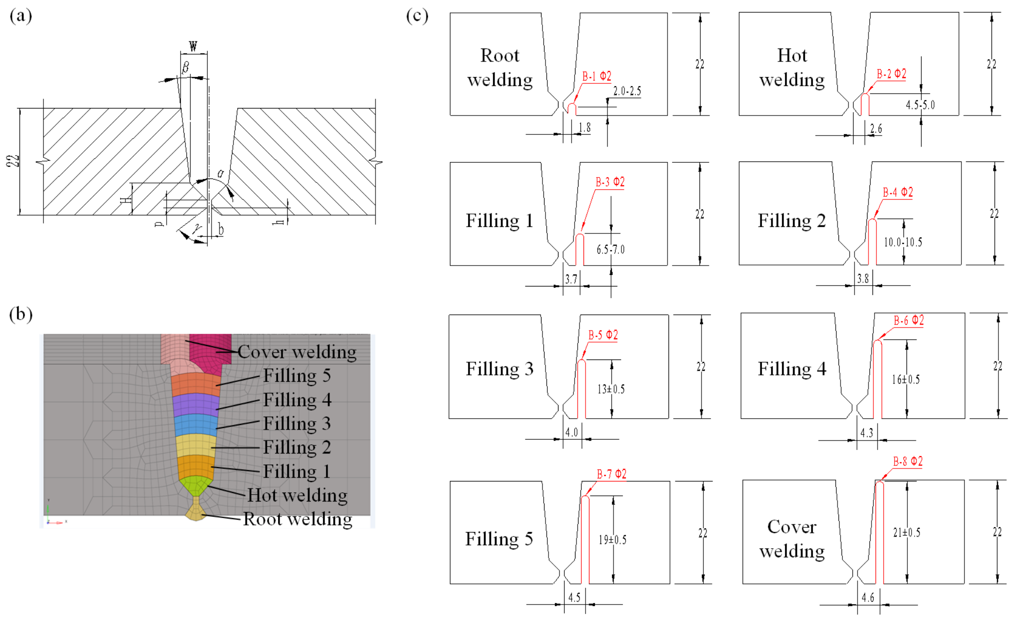

Figure 3. Schematic diagram of the weld groove morphology, welding sequence, and measurement points of the welding thermal cycle curve: (**a**) weld groove morphology, (**b**) welding sequence, (**c**) measurement points of the welding thermal cycle curve.

Table 3. Welding parameters in GMAW.

Welds	Current (A)	Voltage (V)	Wire Feed Speed (m/min)	Shielding Gas Flow Rate (L/min)	Welding Speed (cm/min)	Heat Input (kJ/mm)
Root welding	180–200	22–23	9.0–10	25–28	68	0.36–0.40
Hot welding	190–230	23–25	9.7–10	25–28	53–58	0.49–0.60
Filling 1	185–240	23–25	8.7–10	25–28	36–46	0.65–0.84
Filling 2	185–240	23–25	8.7–10	25–28	36–46	0.65–0.84
Filling 3	180–230	22–25	8.7–9.8	25–28	35–46	0.63–0.80
Filling 4	180–230	22–25	8.7–9.8	25–28	35–46	0.63–0.80
Filling 5	160–225	22–25	8.4–9.5	25–28	38–48	0.59–0.75
Cover welding	120–150	22–24	6.0–6.5	25–28	43–52	0.35–0.44

4.2. Thermophysical Property Testing of Materials

The thermal conductivity and specific heat of the X80 pipeline steel base material and multi-layer welded joint material were measured using the laser flash method. The measurements were conducted using a NETZSCH LFA 457 laser thermal conductivity instrument (NETZSCH Trockenmahltechnik GmbH, Hanau, Germany). To avoid errors caused by individual factors, three round samples of pipeline steel and three round samples of welding wire material were prepared, each with a diameter of 12.7 mm and a thickness of 2 mm. For each temperature point (100 °C, 200 °C, 300 °C, 400 °C, 500 °C, 600 °C, 700 °C, 800 °C, 900 °C), the thermal conductivity and specific heat of both the X80 pipeline steel and welding wire material were measured three times, and the average value of the results was taken as the thermophysical property parameter for that temperature point.

The coefficient of thermal expansion of the X80 pipeline steel base material and multi-layer welded joint material was tested using the NETZSCH DIL 402 high-temperature dilatometer, which was imported from Germany. The temperature range for measurements included 100 °C, 200 °C, 300 °C, 400 °C, 500 °C, 600 °C, 700 °C, 800 °C, and 900 °C. To ensure the accuracy of the test results and minimize the impact of random errors, three specimens were tested, with three sets of data measured at each temperature point. The average values were then taken to plot the curve of the coefficient of thermal expansion as a function of temperature. The thermal expansion coefficient measurement specimen is a cylindrical rod with a length of 25 mm and a diameter of 6 mm.

The elastic modulus and yield strength of the X80 pipeline steel base material and multi-layer welded joint material at different temperatures were measured using the MTS810 universal testing machine and high-temperature tensile testing method. The temperature measurement range for the high-temperature tensile tests of both materials covered several temperature points from room temperature to 900 °C, specifically: 100 °C, 200 °C, 300 °C, 400 °C, 500 °C, 600 °C, 700 °C, 800 °C, and 900 °C. To ensure the accuracy of the test results and minimize the impact of random errors, each test temperature point at high temperatures was measured three times. The three sets of data obtained were required to have good repeatability. If significant differences were found between data points at two test temperatures, an additional test temperature point was added between the three test temperature points to ensure consistency.

4.3. CCT Diagram Measurement, Phase Fraction Statistics, and Hardness Testing

The Gleeble-3500 thermodynamic simulator was used to determine the CCT curve of the X80 pipeline steel weld metal. For the X80 weld samples obtained from the interpass heat treatment tests, the samples were taken in the direction perpendicular to the weld cross-section along the length direction, with the sample center aligned with the center of the weld cross-section. The thermosimulation samples were plate-shaped with dimensions of 11 mm × 11 mm × 80 mm. In a vacuum environment, the samples were subjected to standardized thermosimulation procedures. The temperature was raised at a rate of 200 °C/s to the peak temperature of 1350 °C, held for 1s, and then cooled to room temperature with various cooling rates ($t_{8/5}$ values of 5 s, 6 s, 7.5 s, 10 s, 12.5 s, 15 s, 20 s, 30 s, etc.). The time and corresponding temperature at the inflection points were recorded, and the phase transformation intervals of different phases were determined by the volume changes occurring during the phase transformation process of the specimens.

The overall process of phase fraction testing and hardness testing is shown in Figure 4. First, the hardness testing positions were marked. In this study, the center of each weld seam was divided into three equal parts as the testing points. The hardness of the multi-layer welded joint was measured using a MHV-30A digital Vickers hardness tester. The applied load during the measurement process was 10 kg, and the hardness values at three positions were recorded. The average of these three hardness points was taken as the actual hardness of the weld layer. Subsequently, a sample of 10 mm × 5 mm × 5 mm surrounding the testing points was obtained using electric discharge wire cutting. The sample was polished with water sandpaper to a 2000 # grit and then polished. The microstructure of different weld passes was observed using an GX71 OLYMPUS optical microscope. The microstructure images were imported into Image Pro 6.0 software, where phase differentiation and labeling were performed based on the brightness variation in the field. The phase fractions were obtained by calculating the proportion of different brightness regions.

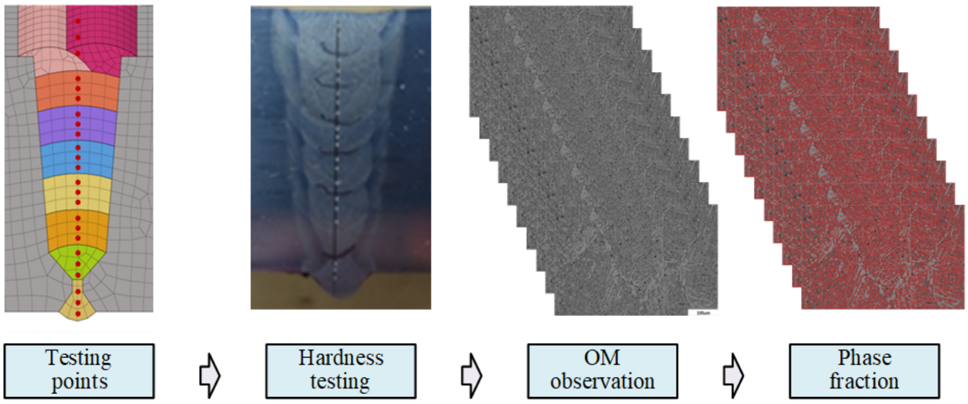

Figure 4. Phase fraction statistics and hardness testing process.

5. Results and Discussion

5.1. Welding Temperature Field Simulation and Thermal Cycle Curve Prediction

Figure 5a shows the welding temperature field of the thermal welding process. The gray area represents the molten pool, and the colored areas represent the unmelted and solidified metal. It can be seen that the welding temperature field only affects a small area around the weld seam. The morphology of the molten pool and the heat-affected zone (HAZ) is compared with the experimental measurement results, as shown in Figure 5b. It can be observed that the molten pool morphology and the heat-affected zone morphology obtained from the finite element simulation fit well with the experimental results, verifying the accuracy of the finite element model. Based on this, the thermal cycle curve at the center point of the bottom of the molten pool is extracted, as shown in Figure 5c. It can be seen that the thermal cycle curve is significantly influenced by the sequential welding passes. Additionally, due to the use of dual welding guns for synchronized off-position welding between filler 1 and filler 2, and between filler 3 and filler 4, the peaks of the thermal cycle curves overlap. The simulated thermal cycle curves of the thermal welding process under different welding conditions are compared with the experimental measurement results. The two results are highly consistent, as shown in Figure 5d, further proving the accuracy of the welding thermal cycle curve simulated using the finite element method.

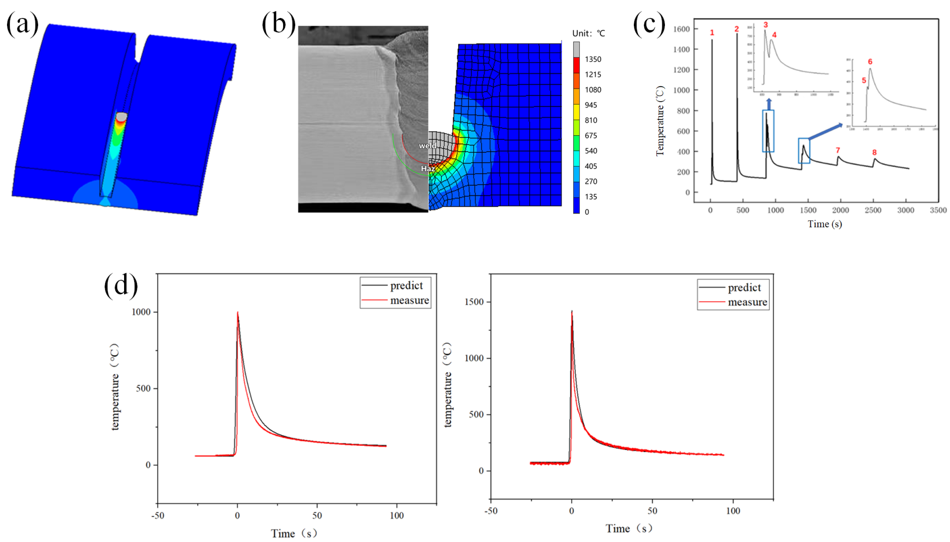

Figure 5. Simulated welding temperature field and its proofread: (**a**) simulated welding temperature field using the finite element method, (**b**) validation of the computational model based on molten pool morphology, (**c**) simulated thermal cycle curve using the finite element method, (**d**) comparison of simulated and measured thermal cycle curves.

Figure 6 shows the prediction results of the cooling section of the welding thermal cycle curve. It can be seen that the curve obtained by predicting feature parameters using the neural network fits well with the FEM calculation results at higher cooling rates, as shown in Figure 6a. However, in the lower cooling rate range, the neural network prediction results are slightly higher than the FEM calculation results. For X80 pipeline steel, the phase transformation interval of the stable phase at room temperature mainly occurs between 500 °C and 800 °C. To balance computational efficiency and accuracy, only the results within this interval can be output, and fitting can be performed using the average cooling rates in the ranges of 500–600 °C, 600–700 °C, and 700–800 °C, as shown in Figure 6b. It can be observed that within the temperature range where phase transformation primarily occurs, the prediction results almost perfectly overlap with the FEM calculation results.

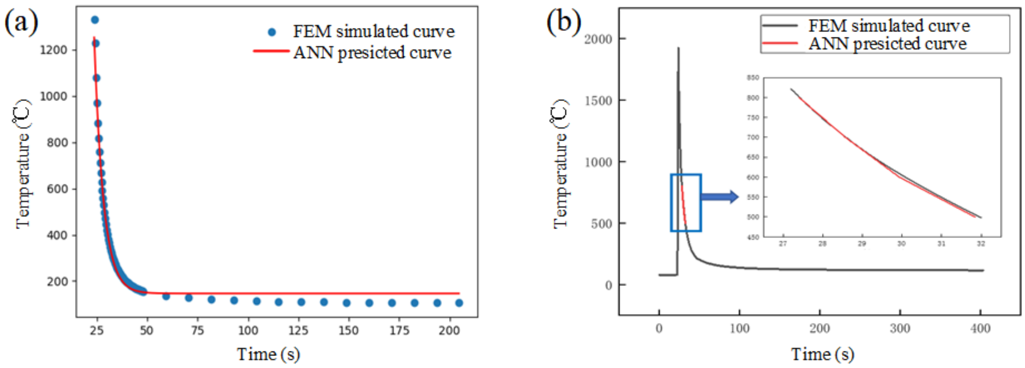

Figure 6. Prediction results of the cooling section of the welding thermal cycle curve: (**a**) Comparison of neural network prediction results with FEM calculation results, (**b**) simplified results of the cooling curve in the phase transformation interval.

5.2. Joint Microstructure and Phase Fraction Prediction

Figure 7 shows the weld microstructure under different welding passes. It can be observed that the joint microstructure is mainly composed of ferrite (represented by white contrast) and pearlite (represented by black contrast). Therefore, the ferrite fraction can be predicted to represent the microstructure information at the measurement location. It is worth noting that due to the differences in welding parameters between different passes, this leads to variations in the welding thermal cycle. Consequently, the ferrite phase fraction does not exhibit a linear relationship between different passes but rather a nonlinear one. This further demonstrates the necessity of constructing a nonlinear relationship model between the thermal cycle information and the microstructure.

Figure 8 shows the CCT curve measurement results and the relationship between the ferrite fraction and cooling rate. Based on the CCT curve, the start and end temperatures of the ferrite phase transformation at different cooling rates can be determined. By combining the CCT curve information from Figure 8a, the values of $P_{eq}(T)$ and $\tau(T)$ can be obtained, as shown in Tables 4 and 5. Additionally, it is observed that as the cooling process $t_{8/5}$ increases, the ferrite fraction generally decreases, as shown in Figure 8. Based on the ferrite fraction at different cooling rates, fitting can be performed for $f(\dot{T})$. The fitting results are shown in Table 6.

Table 4. The $P_{eq}(T)$ interpolation nodes in the Leblond function.

T(°C)	0	500	533	733	780	850	1000
$P_{eq}(T)$	0	0	1	1	0	0	0

Table 5. The $\tau(T)$ interpolation nodes in the Leblond function.

$T(°C)$	0	533	539	597	629	650	671	695	799	801	1000
$\tau(T)$ (s)	10^9	0.6	5.8	3.2	3.5	5.25	4.8	7.6	1000	10^9	10^9

Table 6. The $f(\dot{T})$ interpolation nodes in the Leblond function.

$\dot{T}(°C/s)$	−60	−50	−40	−30	−24	−20	−15	−10
$f(\dot{T})$	0.6	0.46	0.35	0.21	0.16	0.11	0.07	0.035

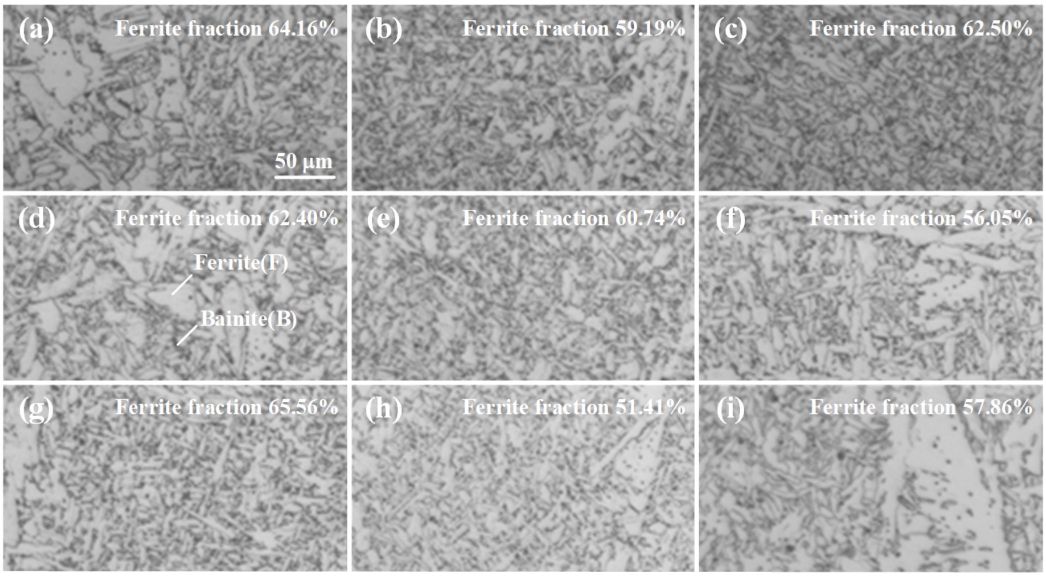

Figure 7. Joint microstructure morphologies and their phase fractions in: (**a**) root welding, (**b**) hot welding, (**c**) filling 1, (**d**) filling 2, (**e**) filling 3, (**f**) filling 4, (**g**) filling 5, (**h**) cover welding 1, (**i**) cover welding 2.

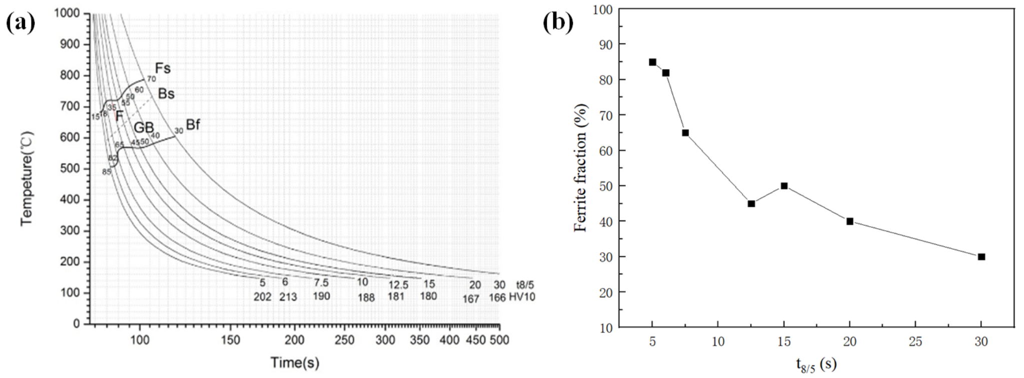

Figure 8. CCT curve measurement results and the relationship between ferrite fraction and cooling rate: (**a**) CCT curve, (**b**) relationship between ferrite fraction and $t_{8/5}$.

By combining the Leblond function with the Leblond parameters in Tables 4–6, the prediction of the ferrite fraction in the joint can be achieved. We randomly selected six sets of results from the hardness test points and predicted their phase fractions. The prediction results are shown in Figure 9. It can be observed that the predicted trend of the ferrite fraction matches the experimental results, with a maximum error of less than 8%, thereby verifying the accuracy of the phase fraction prediction model.

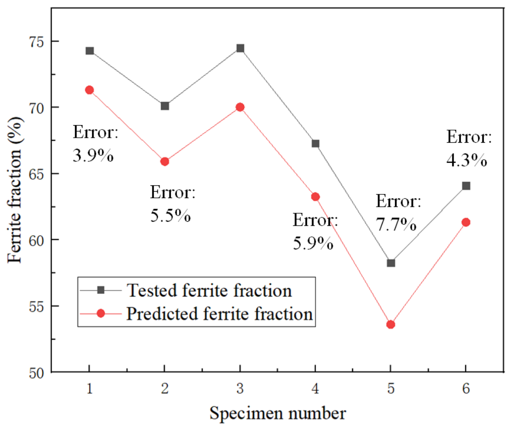

Figure 9. Ferrite fraction prediction results of the joint.

5.3. Joint Hardness Predictions

Figure 10a shows the relationship between joint hardness and ferrite fraction. It can be observed that as the ferrite content increases, the joint hardness generally shows an upward trend. Therefore, it is reasonable to predict joint hardness based on the joint microstructure fraction. The training process MSE curve is shown in Figure 10b. It can be observed that during the training process, the MSE gradually decreases until it is below the expected value. The predicted joint hardness results are shown in Figure 10c. The same samples from Figure 9 are used for hardness prediction, and it is found that the predicted joint hardness results are in good agreement with the experimental measurements, with the maximum prediction error not exceeding 5%. This indicates that the prediction system constructed in this study can achieve accurate prediction of joint hardness.

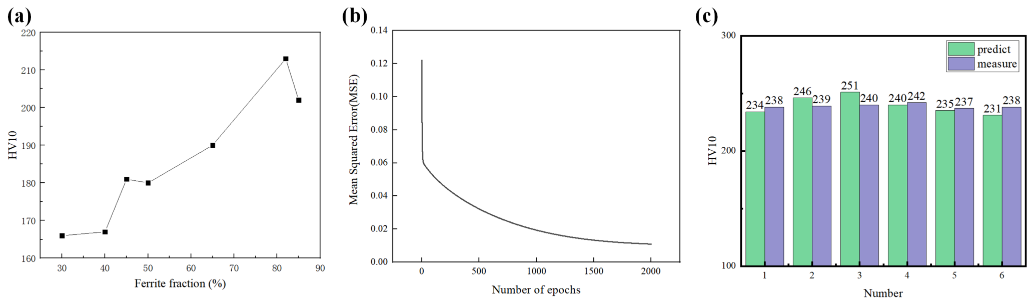

Figure 10. The relationship between joint hardness and ferrite fraction, the training process MSE curve, and the prediction results of joint hardness: (**a**) the relationship between joint hardness and ferrite fraction, (**b**) MSE curve, (**c**) hardness prediction results.

6. Conclusions

In this study, the hardness prediction method of X80 pipeline steel GMAW welded joints was optimized. Starting from the prediction of the welding temperature field, the hardness prediction was finally realized via microstructure prediction. This method can obtain the post-weld hardness based on the hardness essence only using the process parameters. The specific research results are as follows:

1. The thermal cycle curve during welding was obtained via FEM simulations. Its accuracy was validated via comparisons with experimental results. The mapping relationships between the welding parameters and cooling rates were established, and the cooling rate during 500–800 °C could be directly predicted using these parameters.
2. The joint microstructure was mainly composed of ferrite and bainite. Their fractions, decided by the cooling rate, affect joint hardness considerably. By introducing the CCT diagram to the Leblond function, the ferrite fraction can be predicted using the

predicted cooling rates under different welding parameters. The predicted error was less than 8%.

3. The joint hardness was increased with the ferrite fraction. The mapping relationships between joint hardness and the ferrite fraction were built using BP neural networks. By inputting the predicted ferrite fraction from the Leblond function, joint hardness can be obtained with an error of less than 5%.

Author Contributions: Investigation, C.Y.; methodology, H.L.; data curation, D.Y., Y.G. and J.D.; writing—review and editing, Z.Z.; supervision, Z.D. All authors have read and agreed to the published version of the manuscript.

Funding: This study was funded by the China National Petroleum Corporation Science and Technology Development Project 'Research on Intelligent Welding and Detection Technology and Equipment for Long-distance Pipeline', 2021ZG01.

Data Availability Statement: The data presented in this study are available from the corresponding author upon request.

Acknowledgments: We thank Chuanxin XU for help with writing and revising the manuscript. We thank Congcong Tao for providing source codes.

Conflicts of Interest: Chen Yan, Die Yang, and Jun Deng are employed by China Petroleum Pipeline Research Institute Co., Ltd. Yanan Gao is employed by China Petroleum Pipeline Engineering Co., Ltd. The remaining authors declare that this research was conducted in the absence of any commercial or financial relationships that could be construed as potential conflicts of interest.

References

1. Yang, G.; Guo, Z.; Li, Z.; Liang, L.; Zhang, Y.; Guo, H.; Wang, C.; Xu, K.; Li, L. Effect of hydrogen on low-cycle fatigue properties and the mechanism of hysteresis energy method lifetime prediction of X80 pipeline steel. *Corros. Sci.* **2025**, *243*, 112599. [CrossRef]
2. Xue, J.; Cheng, A.; Xia, B. Study on the synergistic effect of welding residual stress and hydrogen diffusion on fatigue crack growth of X80 steel pipeline. *Int. J. Press. Vessel. Pip.* **2024**, *212*, 105367. [CrossRef]
3. Wu, X.; Teng, M.; Jia, W.; Cai, J. Study on the mechanical properties of X80 pipeline steel under pre-charged high-pressure gaseous hydrogen. *Int. J. Hydrogen Energy* **2024**, *84*, 39–52. [CrossRef]
4. Qin, M.; Hu, Q.; Cheng, Y.F. Passivation of X80 pipeline steel in a carbonate/bicarbonate solution and the effect of oxide film on hydrogen atom permeation into the steel. *Int. J. Hydrogen Energy* **2024**, *70*, 1–9. [CrossRef]
5. Garcia, M.P.; Gervasyev, A.; Lu, C.; Barbaro, F.J. Chemical composition and weld cooling time effects on heat-affected zone hardness of line pipe steels. *Int. J. Press. Vessel. Pip.* **2022**, *200*, 104837. [CrossRef]
6. Ning, J.; Yu, Z.S.; Sun, K.; Hu, M.J.; Zhang, L.X.; Zhang, Y.B.; Zhang, L.J. Comparison of microstructures and properties of X80 pipeline steel additively manufactured based on laser welding with filler wire and cold metal transfer. *J. Mater. Res. Technol.* **2021**, *10*, 752–768. [CrossRef]
7. Liu, F.; Tao, C.; Dong, Z.; Jiang, K.; Zhou, S.; Zhang, Z.; Shen, C. Prediction of welding residual stress and deformation in electro-gas welding using artificial neural network. *Mater. Today Commun.* **2021**, *29*, 102786. [CrossRef]
8. Vignesh, P.; Ramanathan, S.; Ramesh, K.; Arockiam, A.J. Finite element modelling to predict hardness of Mg alloy reinforced with Ti/Hydroxyapatite hybrid composites—An axisymmetric approach. *Mater. Today Proc.* **2022**, *68*, 1830–1834. [CrossRef]
9. Murali, B.; Padhi, S.; Patil, C.K.; Kumar, P.S.; Santhanakrishnan, M.; Boopathi, S. Investigation on hardness and tensile strength of friction stir processing of Al6061/TiN surface composite. *Mater. Today Proc.* 2023, *in press*. [CrossRef]
10. Guo, Q.; Pan, Y.; Hou, H.; Zhao, Y. Predicting the hardness of high-entropy alloys based on compositions. *Int. J. Refract. Met. Hard Mater.* **2023**, *112*, 106116. [CrossRef]
11. De Almeida, T.; Nicolau, A.S.; Schirru, R.; Bueno, M. Development of a deep neural network and a PSO algorithm to predict ore hardness using X-ray diffraction and atomic emission spectroscopy. *Miner. Eng.* **2024**, *213*, 108760. [CrossRef]
12. Kasuya, T.; Inomoto, M.; Okazaki, Y.; Aihara, S.; Enoki, M. Hardness prediction for sub-critically and inter-critically reheated HAZs of low alloy steels. *Weld. World* **2023**, *67*, 223–234. [CrossRef]
13. Fang, J.; Li, S.; Dong, S.; Wang, Y.; Huang, H.; Jiang, Y.; Liu, B. Effects of phase transition temperature and preheating on residual stress in multi-pass & multi-layer laser metal deposition. *J. Alloys Compd.* **2019**, *792*, 928–937.
14. Aslam, M.; Sahoo, C.K. Development of hard and wear-resistant SiC-AISI304 stainless steel clad layer on low carbon steel by GMAW process. *Mater. Today Commun.* **2023**, *36*, 106444. [CrossRef]

15. Xiao, L.; Fan, D.; Huang, J.; Tashiro, S.; Tanaka, M. Mild steel metal rotating spray transfer behavior in magnetically controlled gas metal arc welding. *Mater. Today Commun.* **2022**, *31*, 103352. [CrossRef]
16. Mengistie, A.K.; Bogale, T.M. Development of automatic orbital pipe MIG welding system and process parameters' optimization of AISI 1020 mild steel pipe using hybrid artificial neural network and genetic algorithm. *Int. Adv. Manuf. Technol.* **2023**, *128*, 2013–2028. [CrossRef]
17. Vivek Srivastava, B.; Basu, N.P. Application of Machine Learning (ML)-based multi-classifications to identify corrosion fatigue cracking phenomena in Naval steel weldments. *Mater. Today Commun.* **2024**, *39*, 108591. [CrossRef]
18. Ci, Y.; Zhang, Z. Simulation study on heat-affected zone of high-strain X80 pipeline steel. *J. Iron Steel Res. Int.* **2017**, *24*, 966–972. [CrossRef]
19. Murali, B.; Padhi, S.N.; Patil, C.K.; Kumar, P.S.; Santhanakrishnan, M.; Boopathi, S. Effect of welding parameters on weld surface roughness, hardness, and microstructure in laser-welded 340BH-steel and pure vanadium. *Opt. Laser Technol.* **2024**, *175*, 110808.
20. Liu, S.; Shin, Y.C. Prediction of 3D microstructure and phase distributions of Ti6Al4V built by the directed energy deposition process via combined multi-physics models. *Addit. Manuf.* **2020**, *34*, 101234. [CrossRef]
21. Baykasoğlu, C.; Akyildiz, O.; Tunay, M.; To, A.C. A process-microstructure finite element simulation framework for predicting phase transformations and microhardness for directed energy deposition of Ti6Al4V. *Addit. Manuf.* **2020**, *35*, 101252. [CrossRef]
22. Rodgers, T.M.; Moser, D.; Abdeljawad, F.; Jackson, O.D.U.; Carroll, J.D.; Jared, B.H.; Bolintineanu, D.S.; Mitchell, J.A.; Madison, J.D. Simulation of powder bed metal additive manufacturing microstructures with coupled finite difference-Monte Carlo method. *Addit. Manuf.* **2021**, *41*, 101953. [CrossRef]
23. Xiong, F.; Lian, Y.; Panwisawas, C.; Chen, J.; Jian Li, M.; Liu, A. A microscale cellular automaton method for solid-state phase transformation of directed energy deposited Ti6Al4V. *Addit. Manuf.* **2024**, *95*, 104517. [CrossRef]
24. Yang, L.; Yang, J.; Han, F.; Zhang, Z.; Li, Q.; Dong, Z.; Wang, L.; Ofori-Opoku, N.; Provatas, N. Hot cracking susceptibility prediction from quantitative multi-phase field simulations with grain boundary effects. *Acta Mater.* **2023**, *250*, 118821. [CrossRef]
25. Li, Q.; Wang, H.; Zhu, X.; Yang, L.; Liu, B.; Ma, R.; Han, F.; Zhang, Z.; Li, C.; Wang, C.; et al. The combined effects of uniaxial pressure and defects on the mechanism of martensitic transformation in pure iron: A molecular dynamics study. *Mater. Today Commun.* **2024**, *39*, 109092. [CrossRef]
26. Liu, F.; Zhou, S.; Dong, Z.; Jiang, K.; Han, F.; Zhang, Z.; Shen, C. The Prediction of Ferrite Ratio in HAZ of EH36 Steel Electro-Gas Welding Joints Based on Leblond Equation. *Steel Res. Int.* **2022**, *94*, 22002578. [CrossRef]
27. Weisz-Patrault, D. Multiphase model for transformation induced plasticity. Extended Leblond's model. *J. Mech. Phys. Solids* **2017**, *106*, 152–175. [CrossRef]